ChemComm

COMMUNICATION

View Article Online
View Journal | View Issue

Cite this: *Chem. Commun.*, 2025, 61, 7125

Received 18th December 2024,
Accepted 31st March 2025

DOI: 10.1039/d4cc06531j

rsc.li/chemcomm

Enhanced interface electric field in an all-solid-state Z-scheme Ag/AgCl/GCNT heterojunction for facilitating photocatalytic CO_2 reduction performance†

Jintao Dong, ‡[a] Yi Zhang,‡[ab] Lu Liu,[c] Xuemin Zhang,[a] Lina Li,[a] Gaopeng Liu,[d] Huaming Li,[a] Pengcheng Yan*[a] and Jiexiang Xia*[a]

composites of g-C_3N_4 nanotubes with anchored Ag/AgCl nanoparticles (AC/GCNT) were prepared using supramolecular self-assembly and an inert-atmosphere calcination method. The AC/GCNT-2 composites exhibits remarkably enhanced photocatalytic CO generation performance (25.10 μmol g^{-1} h^{-1}) without cocatalysts, hole scavengers, or an organic auxiliary agent, reaching a value 4.41 times that of GCNT materials (5.68 μmol g^{-1} h^{-1}).

The continuous increase of the atmospheric CO_2 concentration can cause global warming, which can affect green-plant growth, ocean circulation directions, and the global distribution of water resources.[1,2] Simultaneously, CO_2 can be considered as a significant C1 resource for further resource utilization and energy development.[3,4] The strategy of CO_2 resource utilization can answer a double purpose: CO_2 emission reduction and clean energy generation.[5] The photocatalytic CO_2 reduction process can realize efficient conversion of solar energy and CO_2 into easily-stored and transportable chemical energy without being driven by other external energy, which is conducive to CO_2 resource conversion and utilization, and large-scale storage of clean energy.[6,7] Nevertheless, the conversion efficiency of the photocatalytic CO_2 reduction process is primarily affected by the high structural stability of the linear CO_2 molecule and the delayed dynamics of photogenerated-carrier migration.[8] Significantly, the construction of efficient photocatalysts is deemed the decisive factor for the photocatalytic CO_2 conversion process, which relies on enhancing the solar-energy conversion efficiency.

Being a non-toxic and inexpensive raw materials, with a large active surface and controllable band structure, g-C_3N_4 has attracted widespread attention and systematic research in the field of photocatalytic CO_2 reduction.[9] Nevertheless, attributed to their π-conjugated structure and non-metallic properties, the internal electric field (IEF) strength and CO_2 activation site numbers of g-C_3N_4 materials should be further optimized *via* various modification strategies.[10,11] The construction of a heterogeneous interface on the surface of g-C_3N_4 nanotube materials has gradually become a common strategy for enhancement of photocatalytic performance by forming efficient electron migration pathways and promoting the directional transport of photogenerated carriers.[12,13] The ability of g-C_3N_4 nanotube materials to separate photogenerated electrons can be effectively enhanced through constructing heterogeneous interfaces on their surfaces *via* coupling with other photo-active materials, which realizes efficient photocatalytic conversion of CO_2.

The morphologies of the GCNT materials, AgCl nanoparticles and AC/GCNT-2 composites were analysed using SEM and TEM measurements. As demonstrated in Fig. S1 (ESI†) and Fig. 1a and b, the GCNT materials exhibits a porous nanotube structure with a diameter of about 200 nm. Furthermore, the size of the AgCl materials obtained *via* a hydrothermal method is from 20 nm to 100 nm (Fig. 1c). As shown in Fig. S2 (ESI†) and Fig. 1d, the AC/GCNT-2 composites still maintains a porous nanotube morphology. Significantly, multitudinous nanoparticles with a diameter of 20 nm are uniformly dispersed on the surface of the AC/GCNT-2 composites. The selected area electron diffraction (SAED) pattern (Fig. 1f) of the AC/GCNT-2 composites indicates the presence of lattice diffraction fringes with spacings of 0.235 and 0.196 nm, corresponding to the Ag (1 1 1) and AgCl (2 2 0) crystalline surfaces, respectively, which demonstrates that Ag/AgCl nanoparticle-loaded GCNT materials were successfully prepared *via* hydrothermal and calcination methods.[14,15] As indicated in Fig. 1g–j, the four elements C, N, Ag and Cl uniformly appear on the surface of the AC/GCNT-2 composites, further demonstrating the uniform distribution of Ag/AgCl nanoparticles on the GCNT materials.

[a] *School of Chemistry and Chemical Engineering, Jiangsu University, Zhenjiang 212013, China. E-mail: yanpengcheng@ujs.edu.cn, xjx@ujs.edu.cn*
[b] *Department of Applied Physics, The Hong Kong Polytechnic University, Kowloon, Hong Kong, 999077, P. R. China*
[c] *Faculty of materials Science and Chemistry, China University of Geoscience, Wuhan 430074, China*
[d] *School of Chemistry and Chemical Engineering of Hainan Normal University, Key Laboratory of Electrochemical Energy Storage and Energy Conversion of Hainan Province, Haikou 571158, China*

† Electronic supplementary information (ESI) available. See DOI: https://doi.org/10.1039/d4cc06531j

‡ These authors contributed equally.

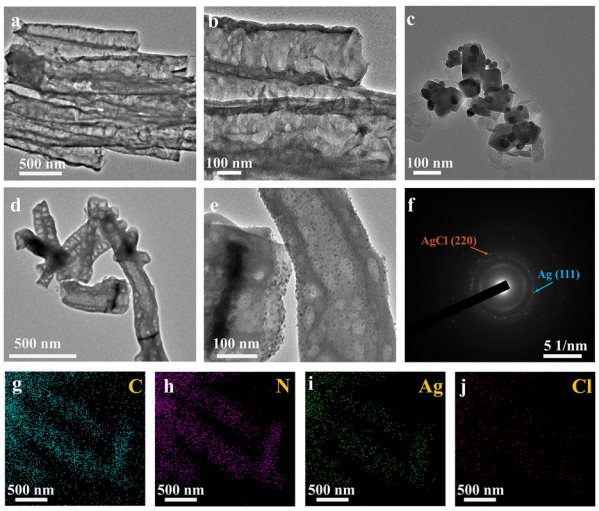

Fig. 1 TEM images of (a) and (b) GCNT, (c) AgCl, (d) and (e) AC/GCNT-2 composites; (f) SAED image and (g)–(j) mapping images of AC/GCNT-2 composites.

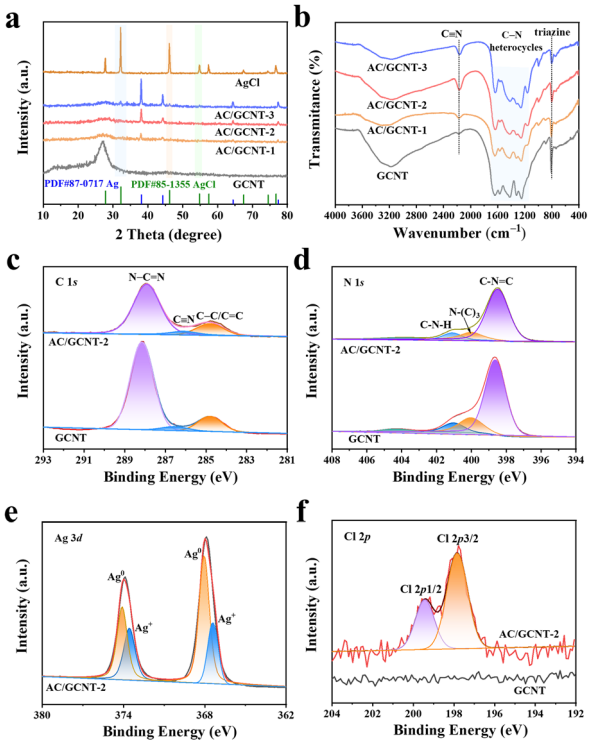

Fig. 2 (a) XRD patterns of GCNT, AgCl and AC/GCNT-*x* composites, and (b) FT-IR spectra of GCNT and AC/GCNT-*x* composites; XPS spectra of GCNT and the AC/GCNT-2 composites: (c) C 1s, (d) N 1s, (e) Ag 3d and (f) Cl 2p.

As shown in Fig. 2a, a conspicuous diffraction peak situated at 27.1° has been observed in the X-ray powder diffraction (XRD) patterns of the GCNT materials, corresponding to the (0 0 2) crystalline plane of the g-C_3N_4 materials. Furthermore, the numerous diffraction peaks located in the XRD patterns of the AgCl materials match with those of cubic AgCl (PDF#85-1355). The diffraction peaks situated at 38.1°, 44.3°, 64.5°, and 77.4° in the XRD patterns of the AC/GCNT-*x* composites correspond to the PDF#87-0717 standard card, indicating the presence of elemental Ag in the AC/GCNT-*x* composites. Furthermore, the weak diffraction peaks corresponding to the AgCl materials are only observed in the AC/GCNT-3 composites, which indicates that further characterization should be carried out to verify the presence of AgCl in the other AC/GCNT-*x* composites. As indicated in Fig. 2b, the characteristic vibrational peaks in the FT-IR spectra of GCNT and the AC/GCNT-*x* composites, located at 808 cm^{-1}, 1200–1700 cm^{-1}, and 2200 cm^{-1}, can be attributed to triazine rings, conjugated C–N heterocyclic structures and –C≡N groups in the GCNT materials.[16–18] A band in the region of 1200 to 1700 cm^{-1} for GCNT and the AC/GCNT-2 composites has been observed (Fig. S3, ESI†), which corresponds to disordered graphitic carbon–nitrogen vibrations.

X-ray photoelectron spectroscopy (XPS) measurements were employed to investigate the chemical composition and elemental valence states of the GCNT and AC/GCNT-2 composites. As demonstrated in the C 1s high-resolution spectra of GCNT and the AC/GCNT-2 composites (Fig. 2c), three characteristic peaks are located at the binding energies of 284.8 eV, 286.7 eV, and 288.0 eV, which corresponds to C–C/C=C, C≡N, and N–C=N bonds, indicating that the Ag/AgCl nanoparticles loading has not caused an obvious impact on the basic structure of the GCNT materials.[19] The N 1s XPS spectra of GCNT and the AC/GCNT-2 composites (Fig. 2d) are Gaussian fitted to three characteristic peaks located at binding energies of 398.6 eV, 400.1 eV, and 401.1 eV, corresponding to the C–N=C bond in C–N heterocycles, and N–$(C)_3$ and C–N–H bonds.[20,21] Furthermore, the high-resolution Ag 3d spectrum of the AC/GCNT-2 composites has been divided into two peaks located at binding energies of 367.4 eV and 373.6 eV, corresponding to the Ag^+ of the AgCl materials. Furthermore, two peaks appear at binding energies of 368.1 eV and 374.1 eV, related to the Ag^0 valence state, suggesting that Ag/AgCl nanoparticles are anchored in the structure of the AC/GCNT-2 composites.[22,23] As indicated in Fig. 2f, an obvious characteristic peak corresponding to Cl^- in the high-resolution Cl 2p spectra has not been observed in the GCNT materials, indicating that the Cl^- in $NH_2OH{\cdot}HCl$ has not been introduced into the GCNT materials. Moreover, the characteristic peaks in the AC/GCNT-2 composites are located at the binding energies of 197.9 eV and 199.5 eV, and are related to the Cl $2p_{3/2}$ and Cl $2p_{1/2}$ orbitals of the AgCl materials.[24,25] The XPS analysis results further indicate that the Ag/AgCl nanoparticles were successfully loaded on the GCNT materials.

The photocatalytic CO_2 conversion performance of the GCNT and AC/GCNT-*x* composite was investigated to evaluate the effect of Ag/AgCl particle introduction under conditions with pure water, no sacrificial agent, and no catalytic additive. The photocatalytic CO generation rate of the GCNT materials (Fig. 3a) reaches 5.68 μmol g^{-1} h^{-1}, and AC/GCNT-*x* composite exhibit a significantly enhanced photocatalytic CO generation ability compared with that of the GCNT materials. The photocatalytic CO generation rates of the AC/GCNT-1, AC/GCNT-2, and AC/GCNT-3 composite reach 12.11, 25.10, and 12.77 μmol g^{-1} h^{-1} (Fig. 3b), which are 2.13, 4.41, and 2.25 times higher than that of the GCNT materials. Compared with previous reports about other C_3N_4-based materials for photocatalytic CO_2 reduction (Table S2, ESI†), AC/GCNT-2

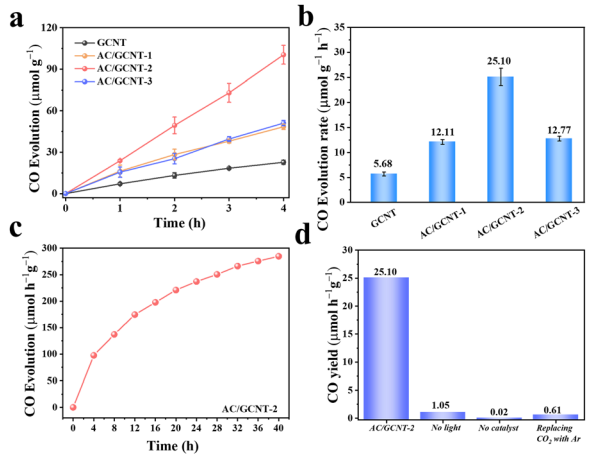

Fig. 3 (a) The photocatalytic CO evolution performance and (b) the photocatalytic CO evolution rate of the GCNT materials and AC/GCNT-*x* composites; (c) the stability of AC/GCNT-*x* composites for photocatalytic CO_2 conversion; (d) the control experiments for the photocatalytic CO evolution rate of the AC/GCNT-2 composites.

composites possesses a high CO evolution rate and selectivity. The continuous photocatalytic CO_2 reduction tests were performed on the AC/GCNT-2 composites to evaluate the reaction stability of the AC/GCNT-2 composites. As shown in Fig. 3c, the photocatalytic CO generation rate of the AC/GCNT-2 composites keeps a continuous increase in a 40 h continuous photocatalytic CO_2 reduction measurement, indicating that the AC/GCNT-2 composites possesses good CO_2 reduction stability. The control experiments (Fig. 3d) indicate that light, the AC/GCNT-2 composites and injecting CO_2 are indispensable reaction conditions for realizing photocatalytic CO_2 conversion.

The transient photocurrent response, electrochemical impedance spectroscopy (EIS) results, photoluminescence (PL) spectra and time-resolved PL (TRPL) decay curves (Fig. S4a–d, ESI†) of the GCNT materials and AC/GCNT-2 composites indicate that the AC/GCNT-2 composites possesses enhanced photogenerated-electron migration efficiency.[26] The distribution model for the electric field was constructed to further elaborate on the IEF enhancement mechanism of the AC/GCNT composites between the GCNT materials and Ag/AgCl nanoparticles (Fig. 4a). As indicated in Fig. 4b and d, a uniform surface electric field distribution has been observed in the GCNT materials, which demonstrates that the electronic transmission efficiency of the GCNT materials needs to be further strengthened.[27] As demonstrated in Fig. 4c, a ''hot spot'' is significantly observed in the centre position of the Ag/AgCl nanoparticles and a remarkable enhanced electric field distribution appears in the interface of the GCNT materials and Ag/AgCl nanoparticles at 470 nm, which indicates that the introduced Ag/AgCl nanoparticles can effectively increase the IEF intensity. Furthermore, the ''hot spot'' appears at the periphery of the Ag/AgCl nanoparticles at 530 nm, which strengthens the

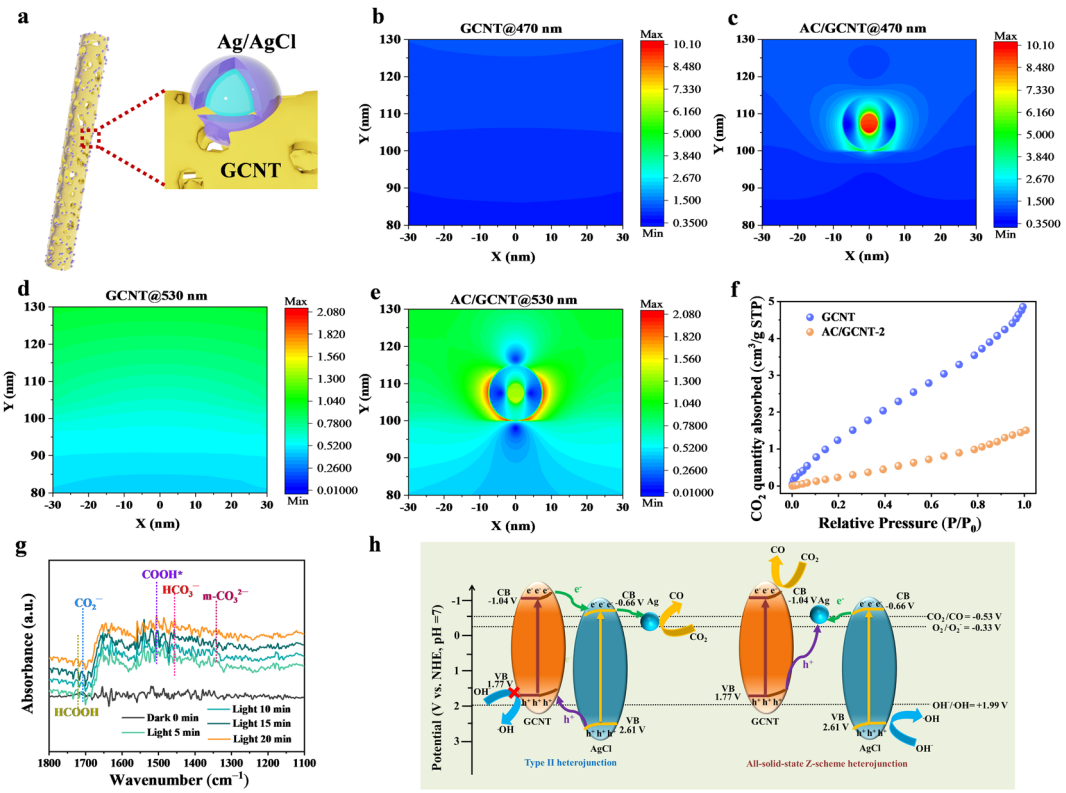

Fig. 4 (a) The schematic diagram of the AC/GCNT-2 composites; the COMSOL simulation results of the GCNT materials at (b) 470 nm and (d) 530 nm, and the AC/GCNT-2 composites with the excitation light wavelength at (c) 470 nm and (e) 530 nm; (f) the CO_2 adsorption isotherm of GCNT and the AC/GCNT-2 composites; (g) *in situ* FT-IR spectra for the photocatalytic CO_2 reduction process of the AC/GCNT-2 composites; (h) schematic illustration of the possible charge transfer mechanism in the AC/GCNT composites.

IEF between the GCNT materials and Ag/AgCl nanoparticles to accelerate electron transport to CO_2 reduction sites. Accordingly, the simulation of the electric field distribution shows that the introduction of Ag/AgCl nanoparticles can achieve efficient migration and utilization of electrons for participation in catalytic CO_2 conversion.

The CO_2 adsorption performance of a photocatalyst is perceived as a considerable evaluation factor for determining the promotion mechanism of the photocatalytic CO generation rate. As indicated in Fig. 4f, the maximum value of CO_2 quantity adsorbed for the GCNT materials is 4.86 cm^3 per g STP, which reaches 3.23-fold that of the AC/GCNT-2 composites (1.50 cm^3 per g STP), further demonstrating that the determining factor is the strengthening of the IEF by heterojunction construction rather than CO_2 adsorption performance. The investigation of intermediate generation in the photocatalytic CO_2 reduction process using *in situ* spectroscopy possesses high research significance and scientific value for analysing the photocatalytic CO_2 reduction process. As observed in Fig. 4g, in the *in situ* FT-IR spectra, the intensity of the vibrational peaks corresponding to *m*-CO_3^{2-} (1347 cm^{-1}), HCO_3^- (1455 cm^{-1}), COOH* (1517 cm^{-1}), CO_2^- (1713 cm^{-1}), and HCOOH (1735 cm^{-1}) intermediates gradually increases with temporal evolution, indicating that the photogenerated electrons continuously interact with CO_2 adsorbed on the AC/GCNT-2 composites to generate reaction intermediates.[28] The energy band structure of the AgCl and GCNT materials has been analysed using $(\alpha h\nu)^2$ *vs.* $h\nu$ curves[29] (Fig. S5a and b, ESI†) and Mott–Schottky plots (Fig. S5c and d, ESI†). Based on electron spin resonance (ESR) spectra (Fig. S6a and b, ESI†) and work-function calculations (Fig. S7a–c, ESI†), an all-solid-state Z-scheme charge transfer mechanism formed by the Ag, AgCl and GCTN materials has been proposed, as shown in Fig. 4h. The TEMPO quenching (Fig. S8a and b, ESI†) and Kelvin probe force microscopy (KPFM) images (Fig. S9a–d, ESI†) further indicate that the AC/GCNT-2 composites possesses high oxidation–reduction ability and spatial distribution of photogenerated carriers.

In summary, composites of g-C_3N_4 nanotubes with anchored Ag/AgCl nanoparticles (AC/GCNT) were successfully constructed. The high-performance directional migration of photogenerated electrons endows the AC/GCNT composites with a high photocatalytic CO_2 reduction rate (25.10 μmol g^{-1} h^{-1}), which is 4.41 times that of the GCNT materials (5.68 μmol g^{-1} h^{-1}). The photogenerated carrier migration path in the all-solid-state Z-scheme AC/GCNT heterojunction formed by the Ag/AgCl nanoparticles and GCNT materials has been revealed by ESR spectra and energy band structure analysis. The simulation of the electric field distribution using COMSOL software and the CO_2 adsorption isotherms of GCNT and the AC/GCNT-2 composites indicate that an intensified IEF strength has a crucial function, rather than CO_2 absorption performance. This manuscript inspires the construction of all-solid-state Z-scheme heterojunctions and contributes a research reference for g-C_3N_4-based composites for photocatalytic CO_2 conversion processes.

This work was financially supported by the National Natural Science Foundation of China (no. 22378172, 22202086).

Data availability

The data used to support the findings of this study are available from the corresponding author upon request.

Conflicts of interest

There are no conflicts to declare.

References

1 H. S. Baker, R. J. Millar, D. J. Karoly, U. Beyerle, B. P. Guillod, D. Mitchell, H. Shiogama, S. Sparrow, T. Woollings and R. A. Myles, *Nat. Clim. Change*, 2018, **8**, 604–608.
2 R. G. Hilton and J. A. West, *Nat. Rev. Earth Environ.*, 2020, **1**, 284–299.
3 E. Orsi, P. I. Nikel, L. K. Nielsen and S. Donati, *Nat. Commun.*, 2023, **14**, 6673.
4 X. L. Zhu, H. B. Zong, C. J. V. Pérez, H. H. Miao, W. Sun, Z. M. Yuan, S. H. Wang, G. X. Zeng, H. Xu, Z. Y. Jiang and G. A. Ozin, *Angew. Chem., Int. Ed.*, 2023, **62**, e202218694.
5 J. T. Dong, S. N. Ji, Y. Zhang, M. X. Ji, B. Wang, Y. J. Li, Z. G. Chen, J. X. Xia and H. M. Li, *Acta Phys. -Chim. Sin.*, 2023, **39**, 2212011.
6 B. Wang, H. L. Chen, W. Zhang, H. Y. Liu, Z. K. Zheng, F. C. Huang, J. Y. Liu, G. P. Liu, X. W. Yan, Y.-X. Weng, H. M. Li, Y. B. She, P. K. Chu and J. X. Xia, *Adv. Mater.*, 2024, **36**, 2312676.
7 L. N. Li, G. P. Liu, S. Q. Cao, J. T. Dong, B. Wang, Y. B. She, J. X. Xia and H. M. Li, *Appl. Catal., B*, 2024, 124904.
8 J. T. Dong, J. Z. Zhao, X. W. Yan, L. N. Li, G. P. Liu, M. X. Ji, B. Wang, Y. B. She, H. M. Li and J. X. Xia, *Appl. Catal., B*, 2024, **351**, 123993.
9 Q. Q. Lu, K. Eid, W. P. Li, A. M. Abdullah, G. B. Xu and R. S. Varma, *Green Chem.*, 2021, **23**, 5394–5428.
10 X. X. Lv, X. M. You, J. Y. Pang, H. Zhou, Z. J. Huang, Y. F. Yao and X. L. Wang, *Chem. Commun.*, 2024, **60**, 4652–4655.
11 S. Hu, P. Z. Qiao, X. L. Yi, Y. M. Lei, H. M. Hu, J. H. Ye and D. F. Wang, *Angew. Chem., Int. Ed.*, 2022, **61**, e202206579.
12 L. Chen, H. Y. Li, H. M. Li, W. S. Qi, Q. Zhang, J. Zhu, P. Zhao and S. D. Yang, *Appl. Catal., B*, 2021, **318**, 121863.
13 W. H. Liu, S. Q. Hu, Y. Wang, B. B. Zhang, R. Y. Jin and G. S. Hu, *Nanoscale Res. Lett.*, 2019, **14**, 108.
14 S. Bera, S. Ghosh and R. N. Basu, *J. Alloys Compd.*, 2020, **830**, 154527.
15 F. Wang, Z. Li, H. H. Wang, M. Chen, C. B. Zhang, P. Ning and H. He, *Nano Res.*, 2022, **15**, 452–456.
16 D. B. Nimbalkar, P. V. R. K. Ramacharyulu, S. R. Sahoo, J. R. Chen, C. M. Chang, A. N. Maity and S. C. Ke, *Appl. Catal., B*, 2020, **273**, 119036.
17 Z. J. Liu, L. Wang, P. F. Liu, K. R. Zhao, S. Y. Ye and G. X. Liang, *Food Chem.*, 2021, **357**, 129753.
18 L. X. Ma, Y. P. Gao, B. Q. Wei, L. Huang, N. Zhang, Q. Weng, L. Zhang, S. Z. Liu and R. B. Jiang, *ACS Catal.*, 2024, **14**, 2775–2786.
19 W. Luo, Y. L. Li, J. S. Wang, J. C. Liu, N. Zhang, M. D. Zhao, J. S. Wu, W. Y. Zhou and L. Z. Wang, *Nano Energy*, 2021, **87**, 106168.
20 Y. Dai, W. R. Peng, Y. Ji, J. Wei, J. H. Che, Y. Q. Huang, W. H. Huang, W. M. Yang and W. Z. Xu, *J. Food Sci.*, 2024, **89**, 8022–8035.
21 Q. Li, Y. Q. Jiao, Y. Q. Tang, J. Zhou, B. G. Wu, B. J. Jiang and H. G. Fu, *J. Am. Chem. Soc.*, 2023, **145**, 20837–20848.
22 D. Sun, Y. Zhang, Y. F. Liu, Z. G. Wang, X. C. Chen, Z. Y. Meng, S. F. Kang, Y. Y. Zheng, L. F. Cui, M. L. Chen, M. D. Dong and B. Hu, *Chem. Eng. J.*, 2020, **384**, 123259.
23 R. Qiao, M. M. Mao, Y. J. Zhong, J. Q. Ning and Y. Hu, *Inorg. Chem.*, 2015, **54**, 9033–9039.
24 Y. T. Yu, Z. J. Zhu, F. Chen, T. Y. Ma and H. W. Huang, *Adv. Mater.*, 2024, **36**, 2413835.
25 F. R. Guo, C. L. Mao, C. Liang, P. Xing, L. H. Yu, Y. Shi, S. B. Cao, F. Y. Wang, X. Liu, Z. H. Ai and L. Z. Zhang, *Angew. Chem., Int. Ed.*, 2023, **62**, e202314243.
26 S. Bera, S. Ghosh, T. Maiyalagan and R. N. Basu, *ACS Appl. Energy Mater.*, 2022, **5**, 3821–3833.
27 D. Sun, J. Mao, H. L. Wei, Q. Zhang, L. Cheng, Z. L. Yang and P. W. Li, *ACS Appl. Mater. Interfaces*, 2022, **14**, 28021–28032.
28 J. Xie, Z. L. Lu, Y. Feng, J. G. Huang, J. D. Hu, A. Z. Hao and Y. L. Cao, *Nano Res.*, 2024, **17**, 297–306.
29 J. J. Lai, L. J. Ding, Y. Liu, C. H. Fan, F. H. You, J. Wei, J. Qian and K. Wang, *Food Chem.*, 2023, **423**, 136285.

